

Wormholing in anisotropic media: Pore-scale effect on large-scale patterns

R. Roded¹, P. Szymczak², and R. Holtzman³

¹Hydrology and Water Resources, The Hebrew University, Jerusalem, Israel

²Institute of Theoretical Physics, Faculty of Physics, University of Warsaw, Warsaw, Poland

³Fluid and Complex Systems Research Centre, Coventry University, Coventry, United Kingdom

Corresponding authors: Piotr Szymczak (piotr.szymczak@fuw.edu.pl), Roi Roded (roi.roded@mail.huji.ac.il)

Contents of this file

Text S1 & S2

Figures S1 & S2

Introduction

The supporting information in this file includes the network model complete description (S1) and results for dissolution of fracture with anisotropically correlated roughness (S2).

Text S1. The Pore Network Model: Detailed Description

1 Model equations and dimensionless groups

1.1 Fluid flow

For an incompressible fluid, the steady-state fluid mass conservation at each node i yields

$$\sum_j q_{ij} = 0, \quad (S1.1)$$

where q_{ij} is the volumetric flow rate through channel ij ($q_{ij} > 0$ indicates flow from node i to j), and the summation is over all neighboring nodes j , linked to node i (Fig. S1a). The channel flow rates are calculated using Hagen-Poiseuille equation

$$q_{ij} = \frac{\pi r_{ij}^4}{8\mu l} \Delta p_{ij}, \quad (S1.2)$$

where r_{ij} is channel radius, μ is fluid viscosity and $\Delta p_{ij} = p_i - p_j$ is the pressure drop between two nodes, which are a distance of l apart (l is assumed to be constant throughout the network). The system of linear equations S1.1 and S1.2 is solved for the pressures at the nodes.

1.2 Reactive transport and dissolution

Dissolution in the cylindrical pores is modeled assuming that: (a) the reaction is characterized by first-order kinetics; (b) reactant transport is controlled by advection in the axial direction, with negligible diffusion; whereas (c) in the transverse (radial) direction the transport and reaction rates are controlled by the diffusion of reactant from the bulk fluid to the mineral surface (Fig. S1b). Condition (b) restricts the analysis to cases in which the Péclet number is sufficiently large, $Pe = \bar{v}l/D \gg 1$, where \bar{v} is the average fluid velocity and D is the molecular diffusion coefficient.

Following assumption (a), the reaction rate at the channel surface is

$$J_r = \lambda c_w, \quad (S1.3)$$

where c_w is the reactant concentration at the wall and λ is the kinetic reaction rate coefficient [L/T]. Reactants at the pore wall are supplied by the diffusion from the bulk fluid. This diffusive flux can be expressed by

$$J_D = h(c - c_w), \quad (S1.4)$$

where c is the flow-weighted average concentration (so-called mixing-cup concentration), defined as $c = \frac{1}{Q} \int_0^r c(\rho) v(\rho) 2\pi\rho d\rho$, with v the fluid velocity and ρ the radial coordinate (Hanna and Rajaram, 1998; Dreybrodt et al., 2005).

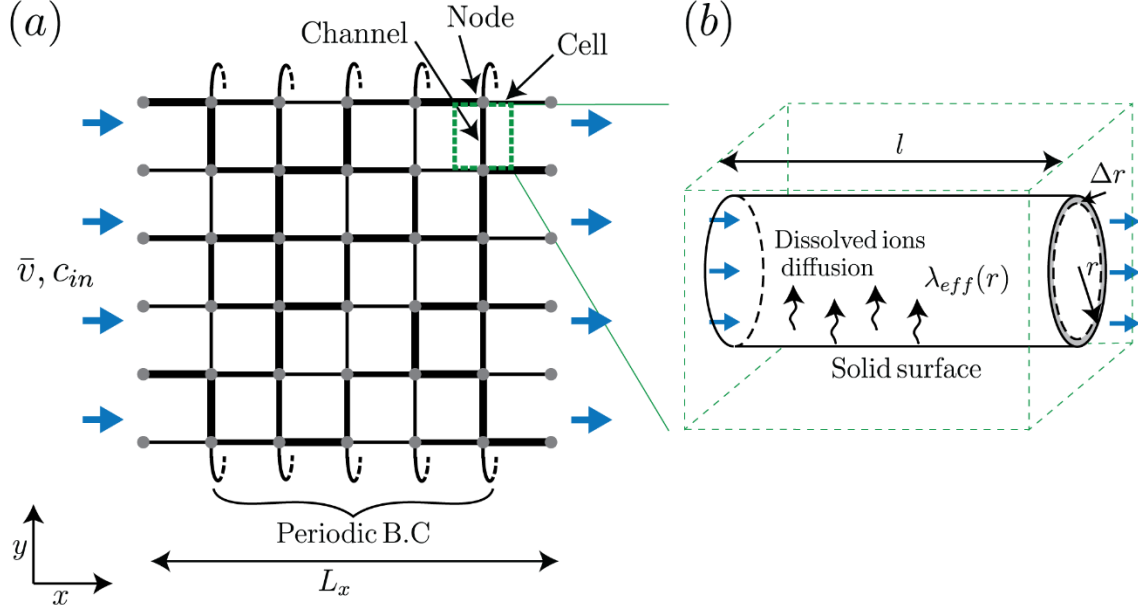


Figure S1. Schematic of the network model. (a) The model comprises 2-D rectangular network of cylindrical channels and nodes (junctions) in a soluble solid. Node i is connected to its neighbor j through channel ij , and heterogeneity is introduced via channel radii. Anisotropy degree, S , is modified by changing the average size of the transverse (y -direction) channels, while the average size of longitudinal channels (in the main flow direction, x) is kept constant. The model cells include the solid volume between respective channels (green frame). Reactive fluid of constant flow rate, Q , and concentration, c_0 , flows from the network inlet face to the outlet face, whereas at the sidewalls periodic boundary conditions are set. (b) The channels are of length l and radius r which changes (by Δr , in gray) following dissolution over a timestep Δt . Reactant diffuses from the fluid bulk to the solid mineral surface. The diffusive flux magnitude is characterized by the mass-transfer coefficient $h(r)$.

The mass-transfer coefficient, h , is inversely proportional to the radius,

$$h(r) = \frac{DSh}{2r}, \quad (S1.5)$$

where Sh is the Sherwood number. Sh depends on λ and is bounded by two asymptotic limits; high reaction rate (transport limit, $Sh=4.364$) and low reaction rate (reaction limit, $Sh=3.656$), respectively (Gupta & Balakotaiah, 2001; Hayes & Kolaczowski, 1994). In our calculations Sh is approximated by a constant, $Sh=4$ (Budek & Szymczak, 2012; Noiriél & Deng, 2018). This assumption is valid as long as the solute entrance length required to

reach the asymptotic value of the Sherwood number, l_{en} , remains small ($l_{en} \ll l$). The entrance length increases with the radius and fluid velocity (see, e.g., Bejan, 2013; Rohsenow et al., 1998). In all our presented simulations, the condition $l_{en} \ll l$ holds.

Once a steady-state is reached, the reactive and the diffusive fluxes (Eqs. S1.3 and S1.4) become equal. This provides an expression for the concentration at the wall in terms of the average concentration, c

$$c_w = \frac{c}{1 + \lambda/h(r)}. \quad (S1.6)$$

Next, expressing the reaction rate (Eq. S1.3) in terms of the average concentration leads to

$$J_r = \lambda^{eff} c, \quad (S1.7)$$

where the effective reaction rate coefficient (Budek & Szymczak, 2012; Noiriél & Deng, 2018), which incorporates both kinetics and transport effects on reaction rate, is

$$\lambda^{eff} = \frac{\lambda}{1 + g(r)}, \quad (S1.8)$$

and

$$g(r) = \frac{\lambda}{h(r)}. \quad (S1.9)$$

The function $g(r)$ is the ratio between the characteristic time-scales of transport $t_d=r/h$ and reaction, $t_r=r/\lambda$, and accounts for the extent by which dissolution rate within a single channel is hindered by transport: for $g \ll 1$ dissolution rate is limited by kinetics, whereas for $g \gg 1$ the reaction is transport-controlled.

Since dissolution in the channels is dominated by advection along the axial direction ξ ($Pe \gg 1$), we obtain 1-D advection-reaction reactant transport equation

$$q \frac{dc}{d\xi} = -2\pi r \lambda^{eff} c. \quad (S1.10)$$

Note that in the above, indices associated with individual channels and nodes (cf. Eqs. S1.1 & S1.2) were omitted for clarity of presentation. For a given reactant concentration at the channel inlet, $c(\xi=0)=c_{in}$, Eq. S1.10 can be solved for the concentration at the channel outlet, $c(\xi=l)=c_{out}$,

$$c_{out} = c_{in} e^{-\frac{s\lambda^{eff}}{q}}, \quad (S1.11)$$

where $s=2\pi rl$ is the channel surface area. Lastly, the concentration of solute at the nodes is calculated from channel outlet concentrations, c_{out} , and solute balance, assuming complete mixing at the channel intersections (Varloteaux *et al.*, 2013; Kang *et al.*, 2019).

Given the reaction rate (Eq. S1.7), the erosion rate of the channels can be calculated based on the mass conservation

$$\frac{\partial r}{\partial t} = \frac{\lambda^{eff}}{\nu c_{sol}} c, \quad (S1.12)$$

where c_{sol} is the molar concentration of soluble solid material and ν accounts for the stoichiometry of the reaction (Detwiler and Rajaram, 2007; Algive *et al.*, 2010). This provides the total volume of mineral dissolved from a single channel surface during a time-step Δt ,

$$\Delta V_{diss} = \frac{2\pi r \Delta t \lambda^{eff}}{\nu c_{sol}} \int_0^l c(x) dx = \Delta t q \frac{c_{in}}{\nu c_{sol}} \left(1 - e^{-\frac{s\lambda^{eff}}{q}}\right). \quad (S1.13)$$

In order to keep the model tractable, we assume that each cylindrical channel dissolves uniformly along its length. The corresponding change in channel radius is then

$$\Delta r = \frac{\Delta V_{diss}}{s} = \frac{\Delta t q}{s} \frac{c_{in}}{\nu c_{sol}} \left(1 - e^{-\frac{s\lambda^{eff}}{q}}\right). \quad (S1.14)$$

The model accounts for a finite amount of soluble solid as follows. If locally—between adjacent channels cells—solid is fully dissolved, channel merging is implemented by increasing the associated hydraulic conductivity (Roded *et al.*, 2018).

1.3 Dimensionless groups characterizing the network evolution

As observed from Eq. S1.11, the decay of reactant concentration between channel inlet and outlet is determined by a function

$$f(r, q) = \frac{s\lambda/q}{1 + g(r)} = \frac{s\lambda^{eff}}{q}, \quad (S1.15)$$

which comprises the ratio between the reactive and advective transport rates. The relative change in radius can then be expressed in terms of the functions f and g (using Eq. S1.14) as

$$\frac{\Delta r}{r_0} = \frac{\Delta \hat{t} c_{in}/c_0}{(1 + g)f} (1 - e^{-f}), \quad (S1.16)$$

where r_0 is the initial average channel radius and \hat{t} is the dimensionless time, defined as

$$\hat{t} = \frac{\lambda t \gamma}{r_0}. \quad (S1.17)$$

Here $\gamma = c_0/c_{sol}V$ is the acid capacity number, defined as the ratio between the number of molecules in a unit volume of a mineral to the number of molecules of the reactant in a unit volume of injected fluid. The dissolution rate of the pores is a function of f and g , with dependence on time arising through the radius, r , and flow rate, q . To characterize transport and reaction conditions, we use initial averaged values of f and g functions for the longitudinal pores aligned in the main flow direction, x . This leads to the following definition of the dimensionless Damköhler number:

$$Da = \frac{s_0 \lambda}{\bar{q}(1 + G)}, \quad (S1.18)$$

and

$$G = \frac{\lambda 2r_0}{DS_h}, \quad (S1.19)$$

where s_0 and \bar{q} are the average surface area and inlet flow rate in longitudinal pores. Note that the Péclet number does not appear in these equations as the diffusive effects in the axial direction are neglected ($Pe \gg 1$).

2 Initial and boundary conditions

We consider the inflow of reactive fluid of constant total volumetric flow rate, Q , and reactant concentration, c_0 , from network inlet face, $x=0$, to outlet face, $x=L_x$, and impose the pressure at the boundaries

$$p(x = 0, y) = p_{in} \quad \text{and} \quad p(x = L_x, y) = 0. \quad (S1.20)$$

As permeability increases in the course of dissolution, to maintain the flow rate, Q , fixed, the pressure at the inlet nodes is adjusted at every time-step. Along with the x (longitudinal) direction, periodic boundary conditions for flow and transport are set, and concentration at the outlet nodes is calculated from solute mass conservation (Eq. S1.11; free-flow boundary).

Text S2. Dissolution of a Fracture with Anisotropically-Correlated Roughness

In this section, we explore the dissolution patterns in a single fracture with an anisotropy introduced by imposing anisotropic spatial correlation lengths of the initial aperture. This is a fundamentally different way of introducing the anisotropy in a dissolving system from that presented in the main text. This difference allows us to examine the sensitivity of our results to the details of the anisotropy model and to test the limitations of the regular pore network model (PNM) in studying wormholing in anisotropic media.

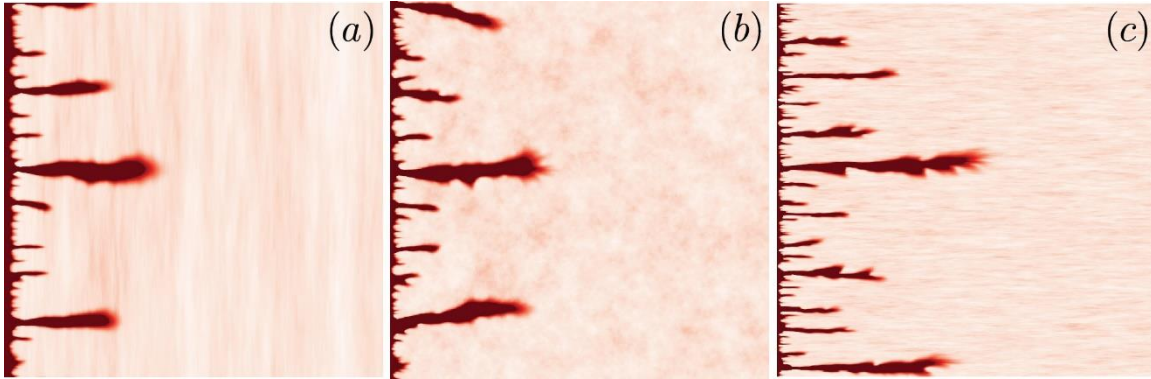


Figure S2. Dissolution patterns in single fracture with anisotropically-correlated aperture. The red color map represents the aperture in the fracture with the correlation lengths (a) $A_y/A_x=10$, (b) $A_y/A_x=1$, (c) $A_y/A_x=0.1$. The system size is $16384b_0 \times 16384b_0$, where b_0 is an initial average aperture. Initial roughness is $R=0.1$ (Eq. S2.4). The Damköhler number is equal to $Da=\lambda\bar{v}=1$ and the Peclet number $Pe=\bar{v}b_0/D=100$.

The model equations of fracture dissolution are based on “depth-averaged” model proposed by Hanna and Rajaram (1998) (see also Detwiler and Rajaram, 2007; Rajaram et al., 2009; Szymczak and Ladd, 2012), in which the fluid velocity and reactant concentration are averaged over the fracture aperture. The depth-integrated fluid flux is calculated based on the Reynolds approximation, whereas the reactant concentration is obtained by solving a depth-averaged advection-diffusion-reaction equation. The details of the particular implementation of this model used in the present study can be found in Upadhyay et al. (2015).

The initial aperture field of the fracture is created by means of the spectral synthesis method (Saupe, 1988), in which one uses a power spectral density of a fracture as a starting point, and then generates the spatially periodic random field with the prescribed spectral density using inverse Fourier transform.

We use a lognormal distribution,

$$\ln(b(x, y)) = W + u(x, y), \quad (S2.1)$$

where $u(x, y)$ is a zero-mean normally distributed random-variable covariance function, $u(x, y)$, of the form (Hanna an Rajaram, 1998)

$$\langle u(x, y)u(x + \delta x, y + \delta y) \rangle = \sigma^2 \exp \left[-\sqrt{\left(\frac{\delta x}{\Lambda_x}\right)^2 + \left(\frac{\delta y}{\Lambda_y}\right)^2} \right]. \quad (S2.2)$$

where Λ_x and Λ_y are the spatial correlation lengths along x and y directions. The mean aperture of such a field is given by

$$\langle b(x, y) \rangle = e^{W + \sigma^2/2}, \quad (S2.3)$$

whereas the mean relative roughness reads

$$R = \frac{\sqrt{\langle b^2 \rangle - \langle b \rangle^2}}{\langle b \rangle} = \sqrt{e^{\sigma^2} - 1}. \quad (S2.4)$$

The results in Fig. S2 demonstrate that decreasing transverse correlation length, Λ_y , leads to a decrease in wormhole spacing, L_s , and an increase in wormhole density, n . The stronger wormhole competition for high transverse correlation length is attributed to the formation of stretched high conductivity regions and strong interaction through the pressure field. This is in full agreement with the PNM results presented in this work, e.g., the corresponding decrease in wormhole spacing and the increase in wormhole density obtained in the network system as anisotropy degree, S , is reduced.

Further, in accordance with our findings from the PNM, for large transverse correlation length (corresponding to large S) substantial wormhole widening downstream is observed (Fig. S2a). This is attributed to the increased flow in the active wormholes as dissolution progresses and as the spacing between them increases. Due to large pressure gradients, the flow spreads sideways from the wormhole tip, leading to widening downstream. The results also demonstrate the tendency to develop side branches for low transverse conductivity (relatively small Λ_y in the fracture model and small S in the network model), where thinner wormholes are obtained (Fig. S2c).

In summary, the qualitative agreement between the results of the PNM and the single fracture model with respect to wormhole density and wormhole shapes demonstrates that the main results and conclusions of this study are insensitive to the details of the pore-scale anisotropy model, and are well captured by the simple representation of a porous medium via the PNM.